Supplemental Figures

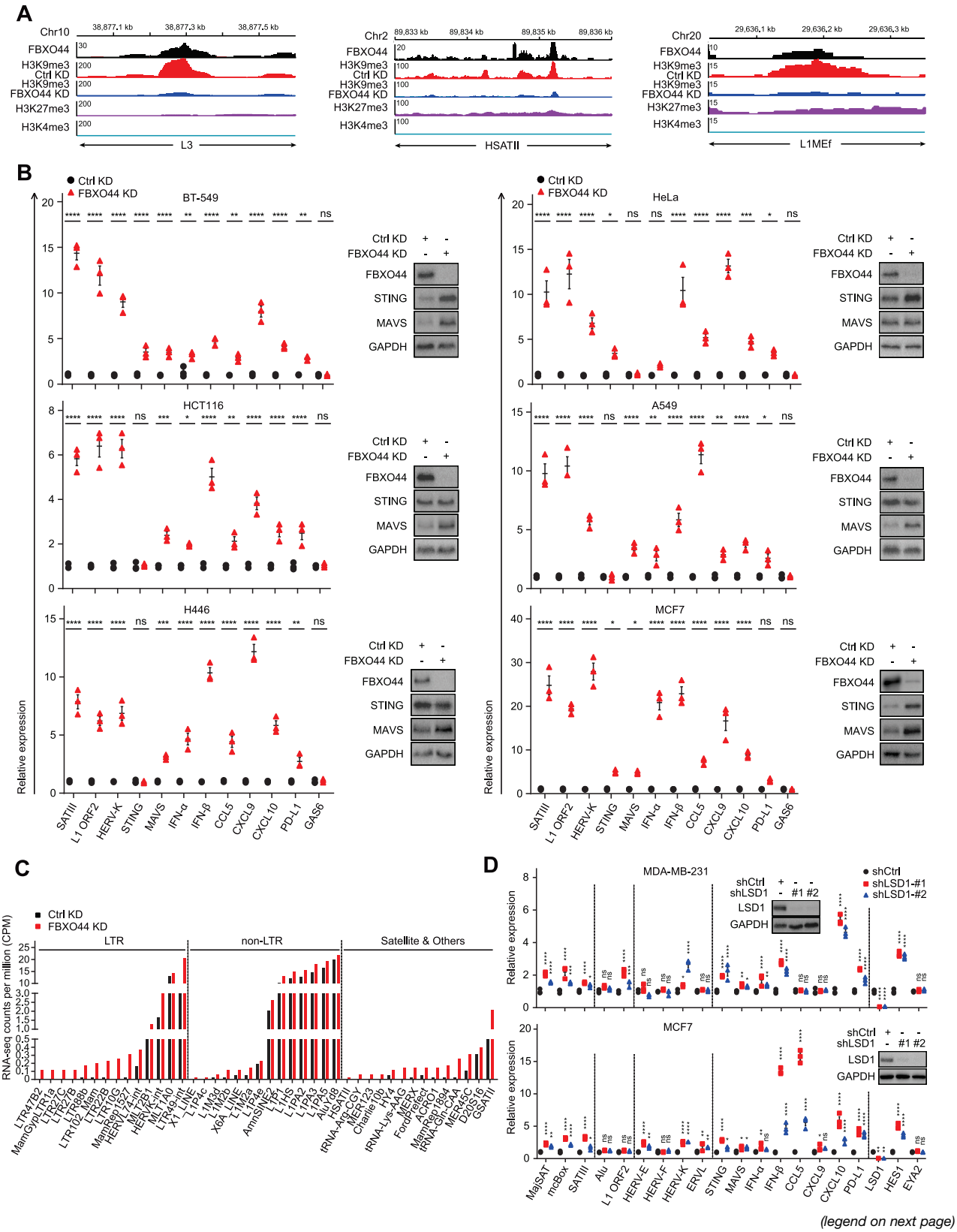

(legend on next page)

Figure S1. FBXO44 regulates H3K9me3-mediated transcriptional silencing of REs in cancer cells, related to Figure 1

(A) Visualization of FBXO44 binding (black) and H3K9me3 modifications (red) on representative genomic regions corresponding to the indicated REs. H3K27me3 and H3K4me3 modifications are also shown.

(B) qRT-PCR analysis of REs, MAVS/STING, IFN-α/β, chemoattractants CCL5, CXCL9, and CXCL10, and PD-L1 in various control and FBXO44 KD cancer cell lines (n = 3) (left panels). GAS6 is control. Immunoblots of the indicated proteins are shown (right panels). GAPDH is loading control.

(C) Analysis of RE transcript levels in RNA-seq data of control and FBXO44 KD MDA-MB-231 cells using RepEnrich2.

(D) qRT-PCR analysis of REs, MAVS/STING, IFN-α/β, chemoattractants CCL5, CXCL9, and CXCL10, and PD-L1 in control and LSD1 KD cancer cell lines (n = 3). HES1 and EYA2 are positive and negative controls, respectively. Immunoblots of the indicated proteins are shown (insets). GAPDH is loading control.

Data represent mean ± SEM. ns, not significant; *p < 0.05, **p < 0.01, ***p < 0.001, ****p < 0.0001 by two-way ANOVA followed by Sidak's multiple comparisons test (B), and Dunnett's multiple comparisons test (D).

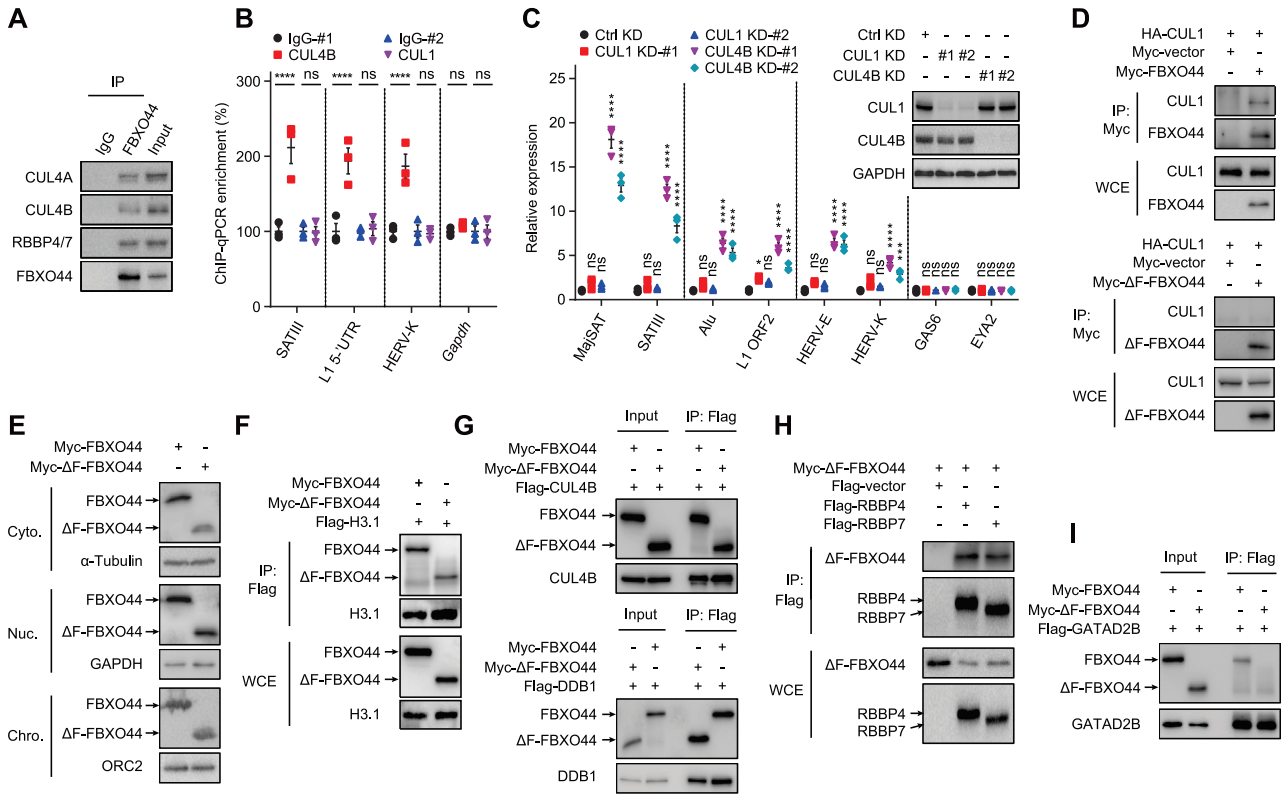

(legend on next page)

Figure S2. FBXO44 recruits SUV39H1, CRL4$^{RBBP4/7}$, and Mi-2/NuRD to REs, related to Figure 2

(A) CoIP of endogenous FBXO44 with CRL4 components CUL4A/CUL4B and DCAFs RBBP4/RBBP7 in MDA-MB-231 cells. IgG is control. Input is 5% of WCE used for IP.

(B) ChIP analysis of CUL1 and CUL4B binding to the indicated REs (n = 3). ChIP was performed with anti-CUL1 or anti-CUL4B antibody. *Gapdh* is control.

(C) qRT-PCR analysis of the indicated REs in control, CUL1 KD, and CUL4B KD MDA-MB-231 cells (n = 3). GAS6 and EYA2 are controls. Immunoblots of the indicated proteins are shown (inset). GAPDH is loading control.

(D) CoIP of Myc-FBXO44 (top panel) or Myc-ΔF-FBXO44 (bottom panel) with HA-CUL1 in MDA-MB-231 cells.

(E) Immunoblots of Myc-FBXO44 and Myc-ΔF-FBXO44 in cytoplasmic, nuclear, and chromatin fractions of MDA-MB-231 cells. α-Tubulin, GAPDH, and ORC2 are fractionation controls.

(F) CoIP of Myc-FBXO44 or Myc-ΔF-FBXO44 with Flag-histone H3.1 in MDA-MB-231 cells.

(G and H) CoIP of Myc-FBXO44 or Myc-ΔF-FBXO44 with CRL4 components Flag-CUL4B (G, top panel) or Flag-DDB1 (G, bottom panel), and Myc-ΔF-FBXO44 with DCAFs Flag-RBBP4/7 (H) in MDA-MB-231 cells.

(I and J) CoIP of Myc-FBXO44 or Myc-ΔF-FBXO44 with Flag-GATAD2B (I) or Flag-SUV39H1 (J) in MDA-MB-231 cells. *, IgG light chain (J).

(K–N) ChIP analysis of binding of the indicated Flag-tagged proteins to various REs in MDA-MB-231 cells transfected with non-targeting or RBBP4+7 siRNAs (K), CUL4B siRNA (L), GATAD2A+B siRNAs (M), or SUV39H1 siRNA (N) (n = 3). ChIP was performed with anti-Flag antibody.

(O) ChIP analysis of H2AK119ub levels at the indicated REs in control and FBXO44 KD MDA-MB-231 cells (n = 3). *Gas6* and *Gapdh* are controls. ChIP was performed with anti-H2AK119ub antibody.

Data represent mean ± SEM. ns, not significant; *p < 0.05, ***p < 0.001, ****p < 0.0001 by two-way ANOVA followed by Tukey's multiple comparisons test (B), Dunnett's multiple comparisons test (C), and Sidak's multiple comparisons test (K-O).

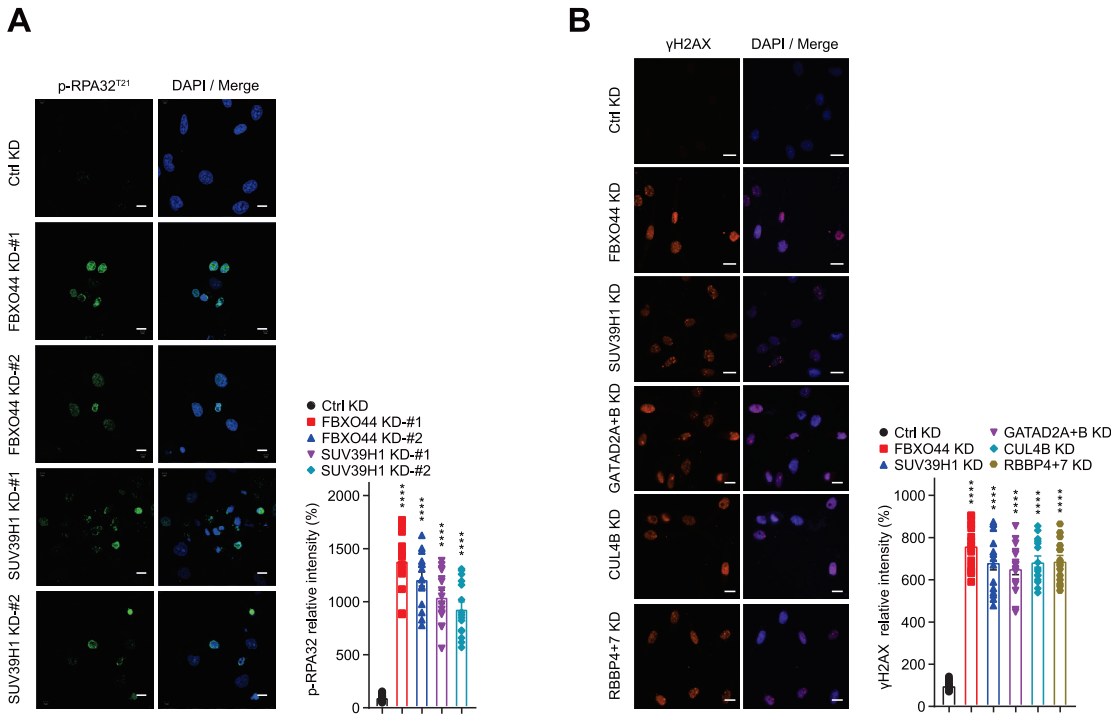

Figure S3. FBXO44/SUV39H1 inhibition promotes DNA replication stress and DSBs in cancer cells, related to Figure 3

(A) IF images of p-RPA32^{T21} in control, FBXO44 KD, and SUV39H1 KD MDA-MB-231 cells (left panel). DNA stained with DAPI. Scale bar, 10 μm. Fifteen cells from 3 different fields (5 for each) were randomly selected and p-RPA32^{T21} quantified using ImageJ (n = 15) (right panel).

(B) IF images of γH2AX in MDA-MB-231 cells transfected with the indicated siRNAs (left panel). DNA stained with DAPI. Scale bar, 10 μm. Fifteen cells from 3 different fields (5 for each) were randomly selected and γH2AX quantified using ImageJ (n = 3) (right panel).

Data represent mean ± SEM. ****p < 0.0001 by one-way ANOVA followed by Tukey's multiple comparisons test (A and B).

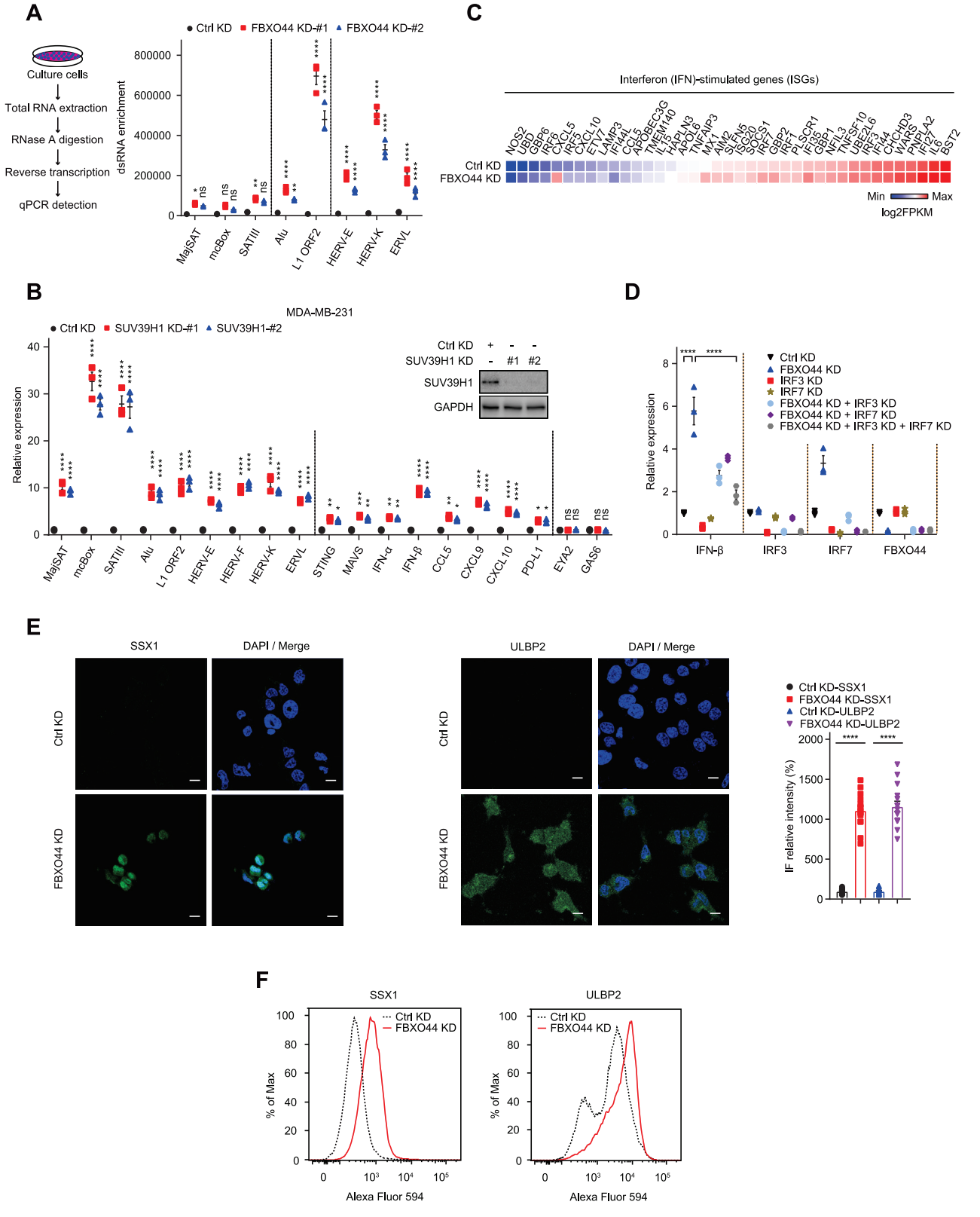

(legend on next page)

Figure S4. FBXO44 inhibition activates RIG-I/MDA5-MAVS and cGAS-STING antiviral pathways and IFN signaling and enhances cancer cell immunogenicity, related to Figure 4

(A) qRT-PCR analysis of the indicated RE transcripts (right panel) in total RNA isolated from control or FBXO44 KD MDA-MB-231 cells and treated with RNase A (n = 3) (left panel).

(B) qRT-PCR analysis of REs, MAVS/STING, IFN-α/β, ISGs, and PD-L1 in control and SUV39H1 KD MDA-MB-231 cells. EYA2 and GAS6 are controls. Immunoblots are shown (inset). GAPDH is control.

(C) Heatmap of differentially expressed ISGs identified by RNA-seq (control KD versus FBXO44 KD).

(D) qRT-PCR analysis of IFN-β in MDA-MB-231 cells transfected with the indicated siRNAs.

(E) IF images (left panels) and quantification of relative intensity (right panel) of CTA SSX1 and NKG2D ligand ULBP2 in control and FBXO44 KD MDA-MB-231 cells. DNA stained with DAPI. Scale bar, 10 μm. Fifteen cells from 3 different fields (5 for each) were randomly selected and quantified using ImageJ (n = 15).

(F) FACS plots of SSX1 and ULBP2 surface expression on control and FBXO44 KD MDA-MB-231 cells in (E).

Data represent mean ± SEM. ns, not significant; $*p < 0.05$, $**p < 0.01$, $***p < 0.001$, $****p < 0.0001$ by two-way ANOVA followed by Dunnett's multiple comparisons test (A and B), Tukey's multiple comparisons test (D), and one-way ANOVA followed by Tukey's multiple comparisons test (E).

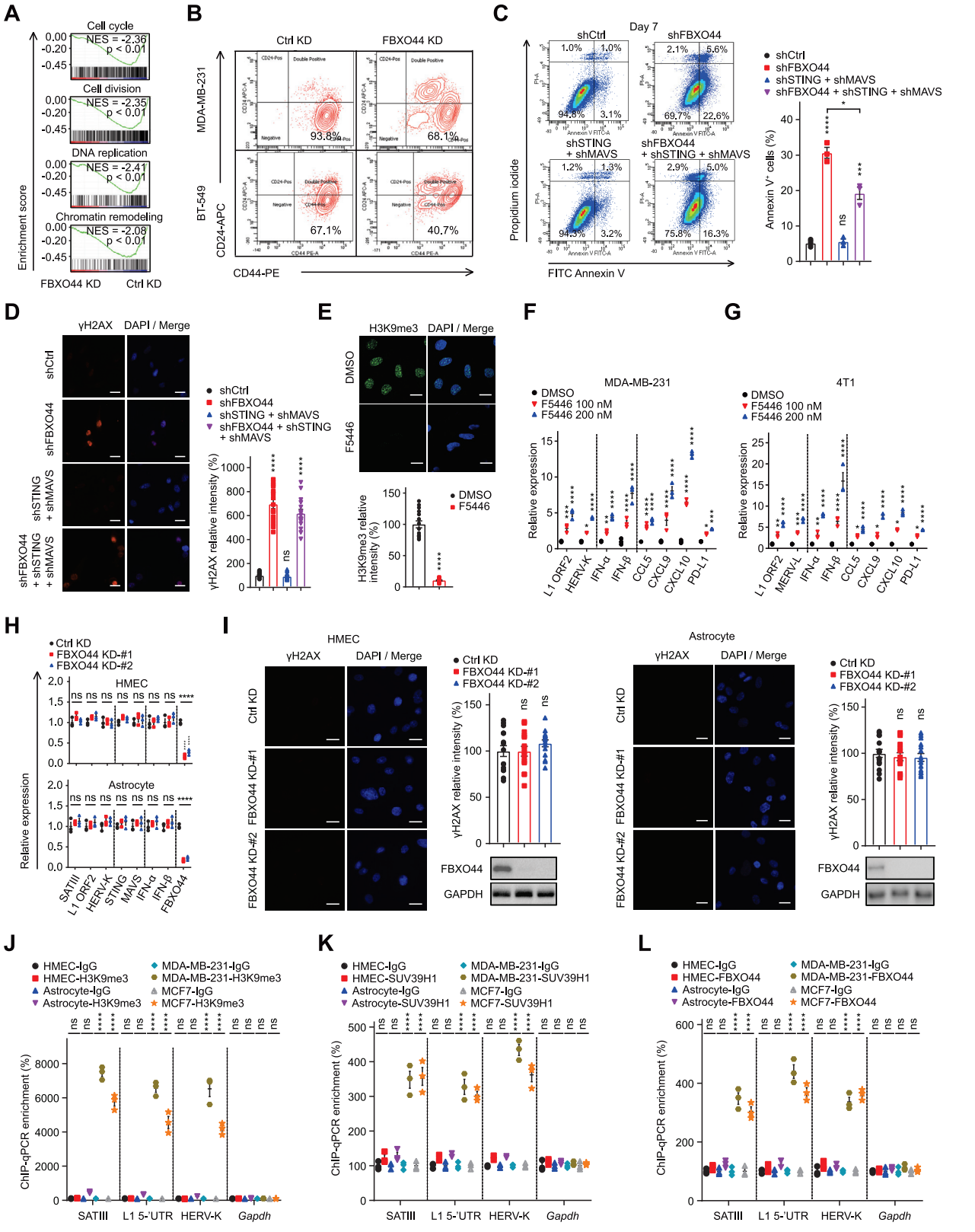

(legend on next page)

Figure S5. FBXO44/SUV39H1 inhibition selectively decreases cancer cell proliferation and viability *in vitro*, related to Figure 5

(A) GSEA enrichment plots for selected gene sets by RNA-seq (FBXO44 KD versus control KD). NES and p values are shown.

(B) Flow cytometry analysis of breast CSCs ($CD24^{low/-}$ $CD44^{+}$) in the indicated control and FBXO44 KD cell lines. The % of CSCs is indicated in each sub-figure.

(C) Flow cytometry analysis of apoptotic (Annexin V^{+}) MDA-MB-231 cells transfected with the indicated siRNAs (left panel). Quantification of the % of Annexin V^{+} cells is shown (n = 3) (right panel).

(D) IF images of γH2AX in MDA-MB-231 cells transfected with the indicated siRNAs (left panel). DNA stained with DAPI. Scale bar, 10 μm. Fifteen cells from 3 different fields (5 for each) were randomly selected and γH2AX intensity quantified using ImageJ (n = 15) (right panel).

(E) IF images of chromatin associated H3K9me3 modifications in MDA-MB-231 cells treated with vehicle or F5446 for 48 hr (left panel). DNA stained with DAPI. Scale bar, 10 μm. Fifteen cells from 3 different fields (5 for each) were randomly selected and H3K9me3 intensity quantified using ImageJ (n = 15) (right panel).

(F and G) qRT-PCR analysis of endogenous retroelements, IFN-α/β, ISGs and PD-L1 in vehicle or F5446-treated MDA-MB-231 (F) or 4T1 cells (G) (n = 3).

(H) qRT-PCR analysis of REs, MAVS/STING, and IFN-α/β in control and FBXO44 KD HMECs and astrocytes (n = 3).

(I) IF images of γH2AX in control and FBXO44 KD HMECs and astrocytes (left panels). DNA stained with DAPI. Scale bar, 10 μm. Fifteen cells from 3 different fields (5 for each) were randomly selected and γH2AX intensity quantified using ImageJ (n = 15) (top right panels). Immunoblots of the indicated proteins is shown (bottom right panels).

(J) ChIP analysis of H3K9me3 levels at the indicated REs in HMECs, astrocytes, and cancer cell lines (n = 3). ChIP was performed with anti-H3K9me3 antibody.

(K) and (L) ChIP analysis of FBXO44 (K) and SUV39H1 (L) binding to the indicated REs in HMECs, astrocytes, and cancer cell lines (n = 3). ChIP was performed with anti-FBXO44 (K) or anti-SUV39H1 (L) antibody.

Data represent mean ± SEM. ns, not significant; *$p < 0.05$, **$p < 0.01$, ***$p < 0.001$, ****$p < 0.0001$ by one-way ANOVA followed by Tukey's multiple comparisons test (A, B, and I), unpaired Student's t test (E), two-way ANOVA followed by Sidak's multiple comparisons test (F-H), and Tukey's multiple comparisons test (J-L).

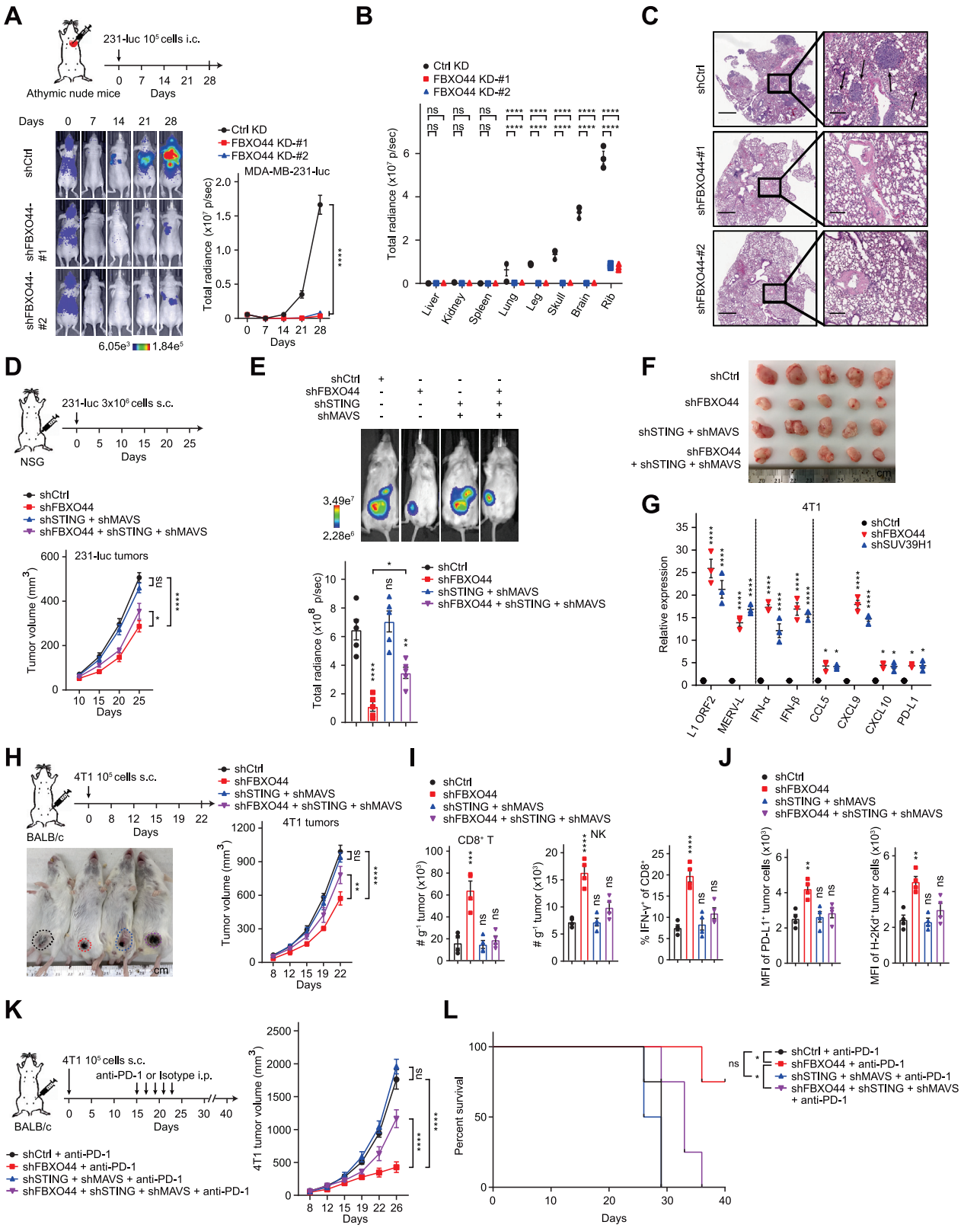

(legend on next page)

Figure S6. FBXO44/SUV39H1 inhibition decreases tumor growth, enhances antitumor immune response, and overcomes resistance to ICB therapy, related to Figure 6

(A) Representative bioluminescent images of immunodeficient mice at the indicated days following intracardiac injection of MDA-MB-231-luc cells expressing non-targeting or 2 different FBXO44 shRNAs (left panel). Plot of total body radiance at the indicated days is shown (n = 8) (right panel).

(B) Total radiance of the indicated tissues isolated from immunodeficient mice in (A) 28 days post-intracardiac injection (n = 3).

(C) Representative images of metastatic lesions (arrows) in lungs of mice in (A). Scale bar, 1 mm; inset scale bar, 200 μm.

(D) Growth curves for MDA-MB-231-luc-derived mammary tumors expressing the indicated shRNAs in immunocompromised mice (n = 5).

(E and F) Representative bioluminescence images (E, top panel) and images of dissected mammary tumors (F) for mice in (D) at day 25. Quantification of total body radiance is shown (n = 5) (E, bottom panel).

(G) qRT-PCR analysis of endogenous retroelements, IFN-α/β, chemoattractants, and PD-L1 in 4T1 cells expressing non-targeting, FBXO44, or SUV39H1 shRNA (n = 3).

(H) Representative images of syngeneic immunocompetent mice with 4T1-derived mammary tumors expressing the indicated shRNAs at day 22 post-transplantation (left panel). Tumor growth curves are shown (n = 4) (right panel).

(I) Flow cytometry quantification of the indicated infiltrating immune cells in 4T1-derived mammary tumors in (H) harvested at day 22 (n = 4).

(J) Flow cytometry analysis of PD-L1 and MHC-I (H-2Kd) surface expression on 4T1 tumor cells in (H). shCtrl (n = 4), shFBXO44 (n = 4), shMAVS+shSTING (n = 4), shFBXO44+shMAVS+shSTING (n = 4).

(K) Growth curves for 4T1-derived mammary tumors expressing the indicated shRNAs in syngeneic immunocompetent mice treated with anti-PD-1 antibody (n = 4).

(L) Survival curves for mice in (K).

Data represent mean ± SEM. ns, not significant; *p < 0.05, **p < 0.01, ***p < 0.001, ****p < 0.0001 by two-way ANOVA followed by Tukey's multiple comparisons test (A, B, D, G, H, and K), one-way ANOVA followed by Tukey's multiple comparisons test (E, F, I, and J), and log-rank test (L).

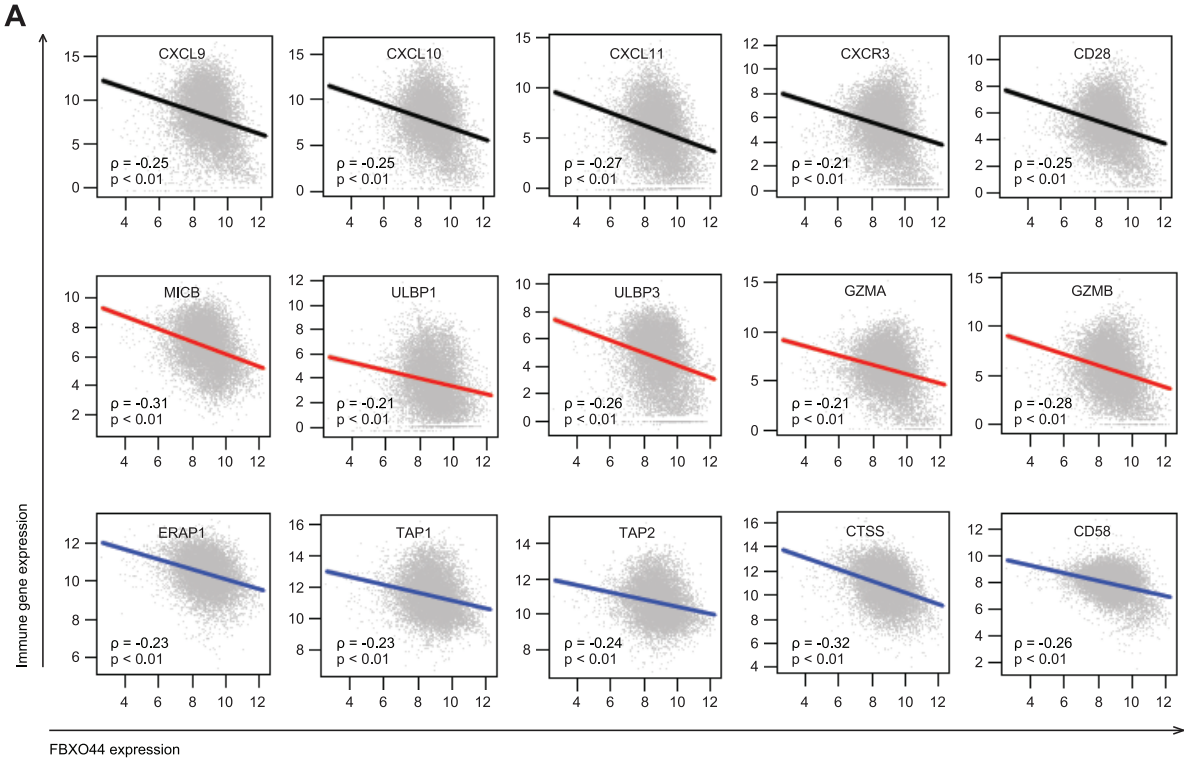

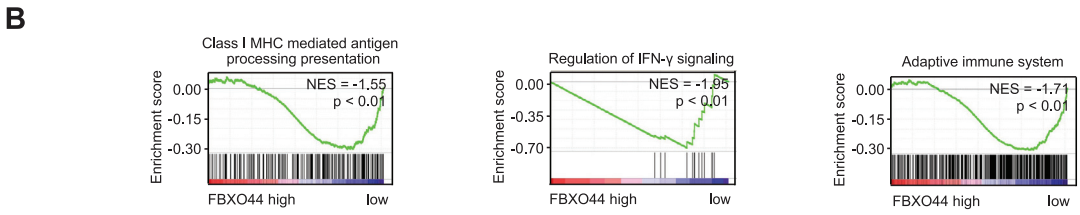

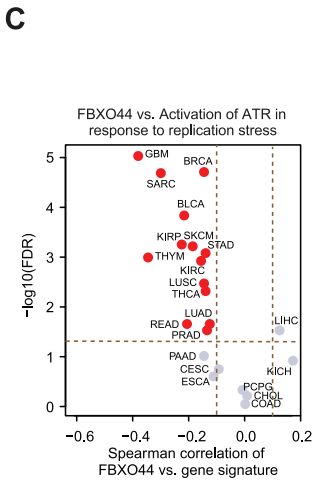

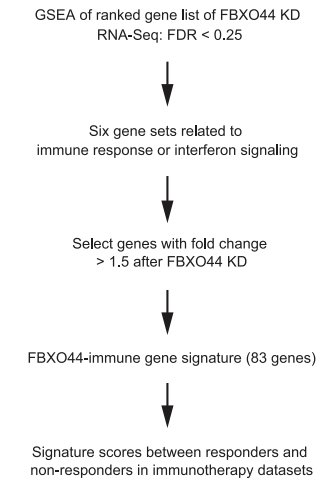

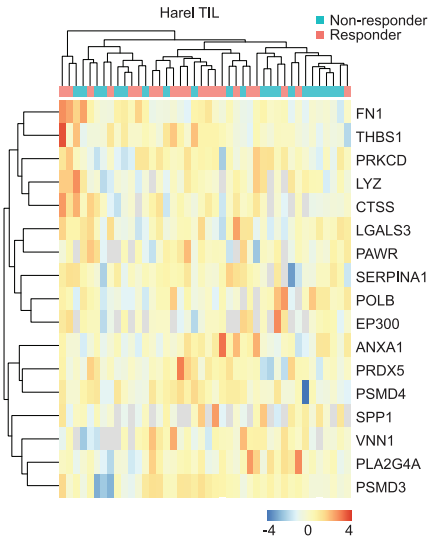

(legend on next page)

Figure S7. FBXO44 is associated with poor clinical outcomes in cancer patient datasets, related to Figure 7

(A) Scatterplots of the expression level correlation between FBXO44 and the indicated representative genes from immune signatures in Figure 7D. The best-fit linear lines, Spearman's ρ, and p values are shown.

(B) GSEA analysis of the indicated immune-stimulatory pathways in FBXO44 high- versus low-expressing tumors in pan-cancer analysis of the TCGA dataset. NES and p values are shown.

(C) Correlation analysis between FBXO44 expression level and z-scores of gene sets for activation of ATR in response to replication stress in different cancer types from the TCGA dataset. p values from Spearman correlation were corrected for multiple testing as FDR.

(D) Generation of FBXO44-immune gene signature (83 immune-related genes) based on GSEA analysis for FBXO44 KD RNA-seq data.

(E) Heatmap of the FBXO44-immune gene signature differentially enriched in responder versus non-responder patients in Harel TIL therapy dataset.